Mechanism and Machine Theory 117 (2017) 21–34

Contents lists available at ScienceDirect

Mechanism and Machine Theory

journal homepage: www.elsevier.com/locate/mechmachtheory

Research paper

A novel 2-DOF compound compliant parallel guiding mechanism

Ke-qi Qi[a,c], Ya-lin Ding[b], Yang Xiang[a,*], Chao Fang[a], Yang Zhang[d]

[a] State Key Laboratory of Applied Optics, Changchun Institute of Optics, Fine Mechanics and Physics, Chinese Academy of Science, Dong_Nanhu Road 3888, Changchun, Jilin 130033, PR China
[b] Key Laboratory of Airborne Optical Imaging and Measurement, Changchun Institute of Optics, Fine Mechanics and Physics, Chinese Academy of Science, Changchun, Jilin 130033, PR China
[c] University of Chinese Academy of Sciences, Beijing 100049, PR China
[d] Research Institute of Zhejiang University-Taizhou, Taizhou, Zhejiang 318000, PR China

ARTICLE INFO

Article history:
Received 31 March 2017
Revised 23 June 2017
Accepted 24 June 2017
Available online 11 July 2017

Keywords:
Compliant
Guiding mechanism
Parasitic displacement
Guiding linearity

ABSTRACT

Based on the analysis of existing guiding mechanisms, a novel 2-DOF compound compliant parallel guiding mechanism (2-DCCPGM) is proposed in this paper, which has compact structure, long motion range and negligible parasitic displacements. The relationship between the guiding displacements and the driving forces have been obtained from the pseudo-rigid-body (PRB) model of 2-DCCPGM. And the dynamic analysis is taken as well. Some design criteria are put forward, based on the analytical results. To analysis the guiding capability and the dynamic performance of 2-DCCPGM, finite element analysis (FEA) has been carried out. And the results of the static FEA simulations confirmed that the 2-DCCPGM barely generates parasitic displacements. A prototype has been manufactured, and experiments have been conducted to validate the performance of the 2-DCCPGM. And from the experimental results, the 2-DCCPGM has been proved to have satisfactory guiding performance. Moreover, the experiment results have also revealed that the machining deviation of the flexure hinges of 2-DCCPGM could cause parasitic displacements and reduce the guiding linearity of the 2-DCCPGM.

1. Introduction

In many precision devices or instruments, the demand for high-precision positioning is growing faster and faster, such as scanning probe microscope, lithography and cell manipulator, etc. [1-5]. Therefore, the development of high-precision positioning stages becomes more and more important in these applications. In general, most of high-precision positioning stages consist two parts: actuators and guiding mechanisms, some of them also have position feedback sensors. Actuators are used to provide the driving force, and guiding mechanisms make sure the stages move in the right path. So, the performance of guiding mechanisms has great impact on positioning accuracy of the stages [6-10]. In recent years, compliant mechanisms become typical guiding mechanisms for high-precision positioning stage, due to the merits in terms of no backlash, no creep, no lubrication requirement, repeatable motion and vacuum compatibility [11-19].

Compliant parallel-guiding mechanism (CPGM) is a classic type of compliant mechanisms [7,20], as shown in Fig. 1a. It is composed of two identical compliant beams and a motion stage, and the compliant beams could be leaf springs or rigid

* Corresponding author.
E-mail address: xiangy@sklao.ac.cn (Y. Xiang).

http://dx.doi.org/10.1016/j.mechmachtheory.2017.06.017
0094-114X/

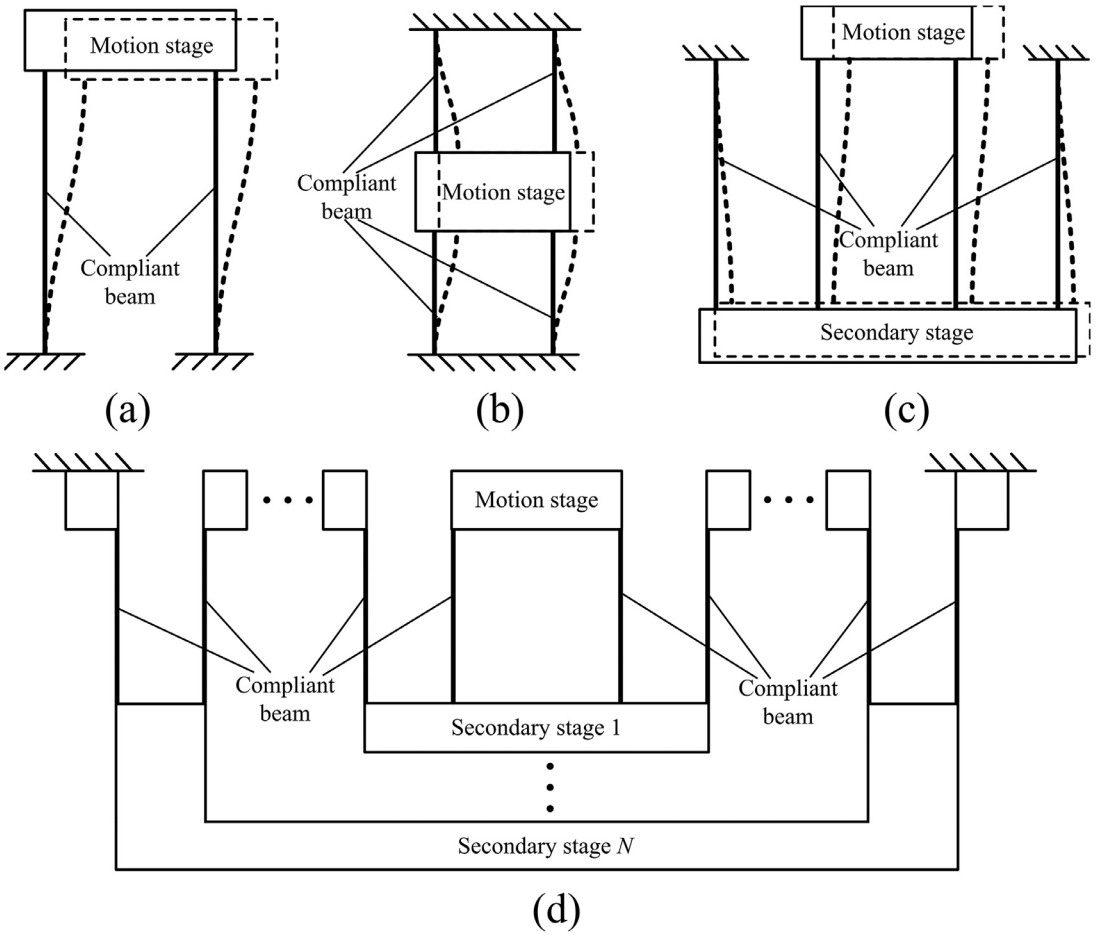

Fig. 1. Schematic of existing 1-DOF compliant mechanisms: (a) CPGM; (b) CDPFM; (c) CPF; (d) MCPF.

beams with flexure hinges at both ends. This type of compliant mechanism has 1-DOF translational motion capability. CPGM takes advantage of the principle that each set of opposite sides of parallelogram mechanism always remains parallel. And it makes the motion stage of CPGM barely have angular displacement during the whole procedure of deformation. But there is an obvious drawback that the parasitic translation would cause undesired displacement in the vertical direction, and the guiding linearity and positioning accuracy of stages would be reduced, especially in the case of large deformation. To solve this problem, researchers introduced compliant double parallel four-bar mechanism (CDPFM) [21]. CDPFM is actually composed of two symmetrically and parallelly arranged CPGMs, as shown in Fig. 1b. This form of structure effectively avoided the parasitic translation which occurred in CPGM, thus the guiding linearity is significantly improved. Nevertheless, such an over-constrained structure would limit the motion range of CDPFM. To avoid the parasitic translation occurred in CPGM, a simple compound linear spring with monolithic flexure hinges was adopted [22]. Awtar [23] introduced compound parallelogram flexure (CPF) and designed a totally decoupled XY parallel stage by using this mechanism. The CPF is composed of two reversely and serially arranged CPGMs, as shown in Fig. 1c. From Fig. 1c, it can be seen that the parasitic translation of the motion stage is counteracted by the parasitic translation of the secondary stage. So, the guiding linearity of CPF is desirable, and the motion range is doubled as compared to CPGM. Inspired by CPF, the concept of multi-stage compound parallelogram flexure (MCPF) is proposed to achieve a larger translational motion [24]. The MCPF is composed of a number of CPFs which are nested layer by layer, as shown in Fig. 1d. From Fig. 1d, the first CPF can be considered as the motion stage of the second CPF, the second CPF can be considered as the motion stage of the third stage, and go on like this. The motion range of MCPF is N times as long as that of the adopted CPF, where N is the number of adopted CPFs. MCPF has all advantages of CPF, and its motion range could be increased by adopting more CPFs. However, the above-mentioned guiding mechanisms only have 1-DOF translational motion capability, people have to combine these mechanisms together in serial, parallel or hybrid to achieve 2-DOF or 3-DOF translational motion capability [25-27]. But in some applications, these mechanisms are not practical. Therefore, researchers introduced multi-axis flexure hinges into these compliant mechanisms. Bacher applied 2-axis flexure hinges into CPGM to possess 2-DOF guiding capability [28], as shown in Fig. 2a. Xu [29] designed a 2-DOF spatial stage by adopting 2-axis flexure hinges into CPF, as shown in Fig. 2b. However, these two mechanisms cannot

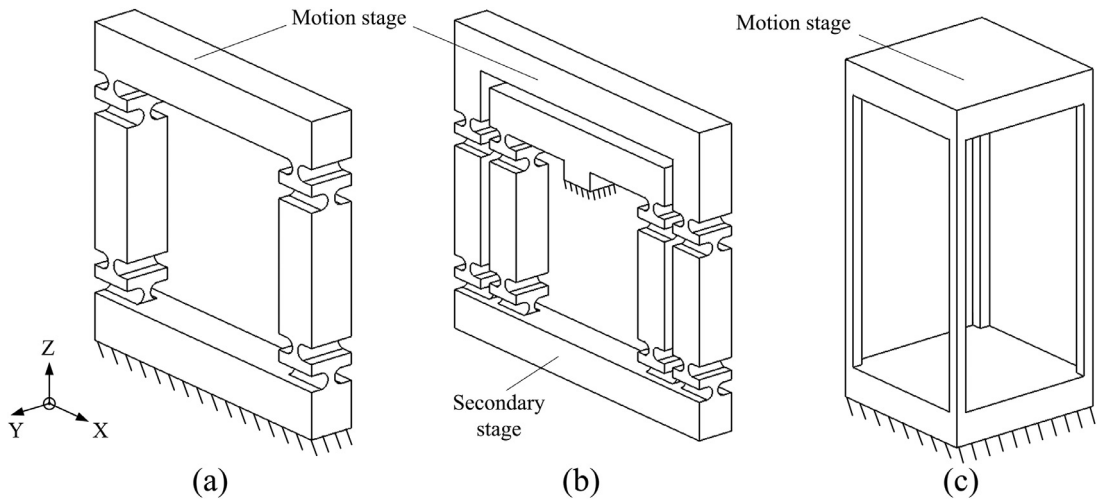

Fig. 2. Schematic of existing 2-DOF compliant mechanisms: (a) 2-DOF CPGM; (b) 2-DOF spatial stage; (c) FBCM.

achieve 2-DOF translations without parasitic rotations and translations on their own, and the reason will be discussed in the next section. Li and Hao [30] introduced a four-beam compliant module (FBCM) into an XYZ compliant parallel mechanism, as shown in Fig. 2c. But this mechanism has the parasitic translation problem just like CPGM. Therefore, it is necessary to develop a new mechanism, which has 2-DOF guiding capability, negligible parasitic motions and compact structure.

This paper proposes a novel 2-DOF compound compliant parallel guiding mechanism, which has compact structure, long motion range and negligible parasitic displacements. The remaining parts of this paper are organized as follows. Section 2 introduces the design procedure and analytical modeling of 2-DCCPGM. In Section 3, a 3-D model is built. FEA simulations are taken in Section 4. In Section 5, a prototype is fabricated, and series of experimental studies are carried out to validate the performance of 2-DCCPGM. Concluding remarks are summarized in Section 6.

2. Mechanism design

2.1. Design of 2-DCCPGM

As mentioned above, the 2-DOF spatial stage has the defect of parasitic rotation and translation, and the reason will be discussed in this section. A 2-DOF spatial stage with universal flexure hinges is depicted in Fig. 3a, and its PRB model is shown in Fig. 3b. There is no doubt that the 2-DOF spatial stage scarcely has parasitic displacements as guiding in X-axis, so we should only discuss the parasitic displacements which occur as the stage is guiding in Y-axis. In order to distinguish the motion stage from the secondary stage clearly, a certain distance is kept between these two stages along the Y-axis in the PRB model of 2-DOF spatial stage, as shown in Fig. 3b. Fig. 3c shows the deformation of the 2-DOF spatial stage when a horizontal force $2F$ is applied on the motion stage. Fig. 3d shows the force status of the motion stage and the secondary stage, respectively. From Fig. 3d, it can be seen that the load of the secondary stage consists a force $2F$ and a moment $2M$. And M can be derived from:

$$M = F(L + 2l). \tag{1}$$

And then, the rotation angles of the flexure hinges of the secondary stage can be derived from following equations:

$$\varphi_1 = \frac{M - F(l+L)}{K_\varphi} = \frac{Fl}{K_\varphi}, \varphi_2 = \varphi_1 + \frac{M - Fl}{K_\varphi} = \frac{M}{K_\varphi} = \frac{F(2l+L)}{K_\varphi} \tag{2}$$

where K_φ is the rotational stiffness coefficient of the universal flexure hinges of the 2-DOF spatial stage along X-axis. The rotation angles of flexure hinges of the motion stage can also be derived from following equations:

$$\varphi_3 = \varphi_2 + \frac{F(l+L)}{K_\varphi} = \frac{F(3l+2L)}{K_\varphi}, \varphi_4 = \varphi_3 + \frac{Fl}{K_\varphi} = \frac{2M}{K_\varphi} = \frac{2F(2l+L)}{K_\varphi}. \tag{3}$$

Then, the parasitic translation of the 2-DOF spatial stage, which is δ in Fig. 3d, can be obtained:

$$\delta = l + L\cos\varphi_1 - L\cos\varphi_3 - l\cos\varphi_4. \tag{4}$$

If a moment $2M_o$ is added on the motion stage along X-axis, then Eqs. (2) and (3) can be written as follows:

$$\varphi_1' = \frac{M_o - Fl}{K_\varphi}, \varphi_2' = \varphi_1' + \frac{M_o - F(l+L)}{K_\varphi} = \frac{2M_o - F(2l+L)}{K_\varphi} \tag{5}$$

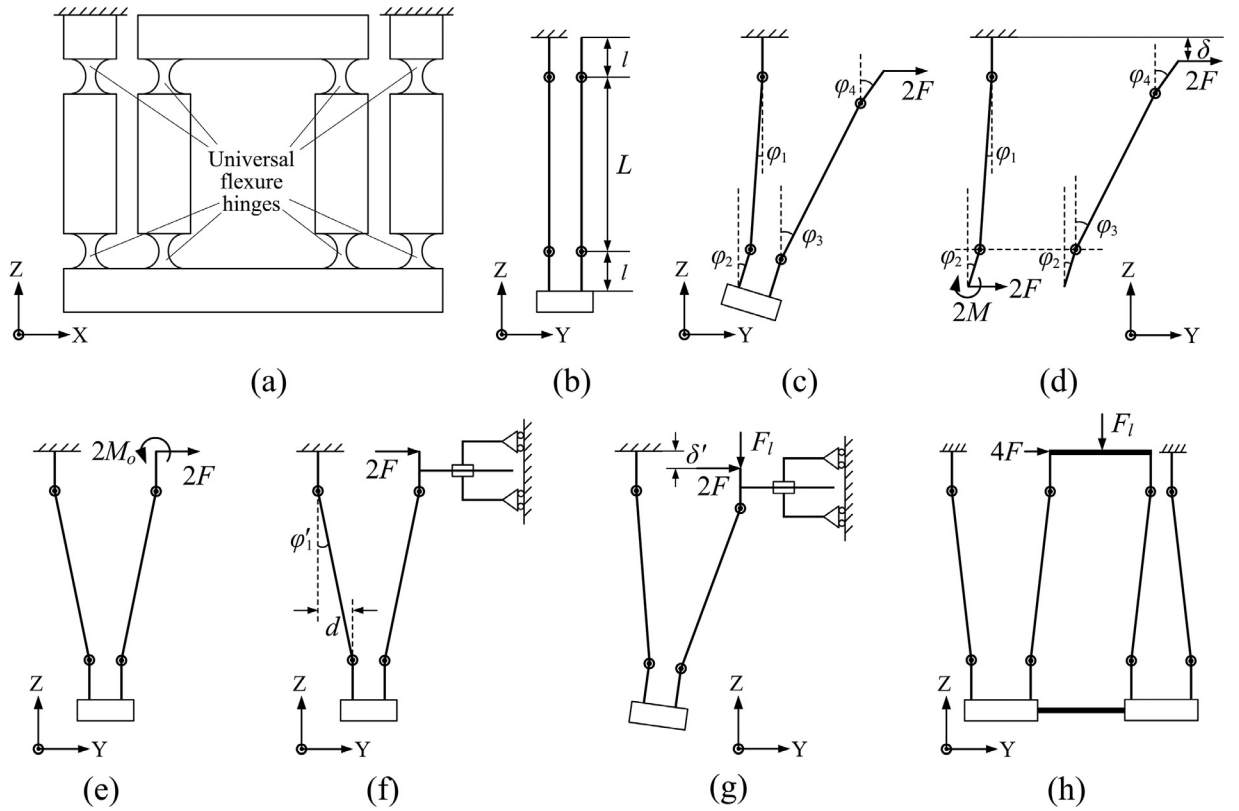

Fig. 3. The schematic and PRB model of 2-DOF spatial stage: (a) schematic of 2-DOF spatial stage; (b) PRB model of 2-DOF spatial stage; (c) the deformation of the 2-DOF spatial stage when a horizontal force 2*F* is applied on the motion stage; (d) the force status of the motion stage and the secondary stage; (e) a proper moment $2M_o$ is added on the motion stage along X-axis; (f) the moment $2M_o$ is substituted by a rotational constrain; (g) the deformation of the 2-DOF spatial stage when a load F_l is applied on the motion stage; (h) the motion stages and secondary stages of two identical 2-DOF spatial stages are connected, respectively.

$$\varphi'_3 = \varphi'_2 + \frac{M_o - F(l+L)}{K_\varphi} = \frac{3M_o - F(3l+2L)}{K_\varphi}, \varphi'_4 = \varphi'_3 + \frac{M_o - Fl}{K_\varphi} = \frac{4M_o - F(4l+2L)}{K_\varphi} \tag{6}$$

where φ'_1, φ'_2, φ'_3 and φ'_4 are the rotation angles of flexure hinges of the 2-DOF spatial stage after $2M_o$ is added.

From Eq. (6), if we make φ'_4 equal to zero, M_o can be obtained:

$$\varphi'_4 = \frac{4M_o - F(4l+2L)}{K_\varphi} = 0 \Rightarrow M_o = \frac{F(2l+L)}{2}. \tag{7}$$

Substituting Eq. (7) into Eqs. (5) and (6), the other rotation angles of flexure hinges of the 2-DOF spatial stage can be derived:

$$\varphi'_1 = \frac{M_o - Fl}{K_\varphi} = \frac{FL}{2K_\varphi}, \varphi'_2 = \frac{2M_o - F(2l+L)}{K_\varphi} = 0, \varphi'_3 = \frac{3M_o - F(3l+2L)}{K_\varphi} = \frac{-FL}{2K_\varphi}. \tag{8}$$

From Eqs. (4) and (8), the parasitic translation of the 2-DOF spatial stage can be derived:

$$\delta' = l + L\cos\varphi'_1 - L\cos\varphi'_3 - l\cos\varphi'_4 = l + L\cos\frac{FL}{2K_\varphi} - L\cos\frac{FL}{2K_\varphi} - l\cos 0 = 0. \tag{9}$$

From Eq. (9), it can be seen that the parasitic translation and rotation of the 2-DOF spatial stage can be eliminated by adding a proper moment $2M_o$ along X-axis, as shown in Fig. 3e. It means that the 2-DOF spatial stage needs an additional moment $2M_o$ to achieve translational motion without parasitic displacements in Y-axis, and M_o are proportional to *F*. Based on above analysis, it is easy to notice that moment $2M_o$ could be substituted by a rotational constrain, as shown in Fig. 3f. And from Fig. 3f, the guiding displacement of the 2-DOF spatial stage is

$$D_1 = 2d = 2L\sin(\varphi'_1) = 2L\sin(\frac{FL}{2K_\varphi}) \approx \frac{FL^2}{K_\varphi}. \tag{10}$$

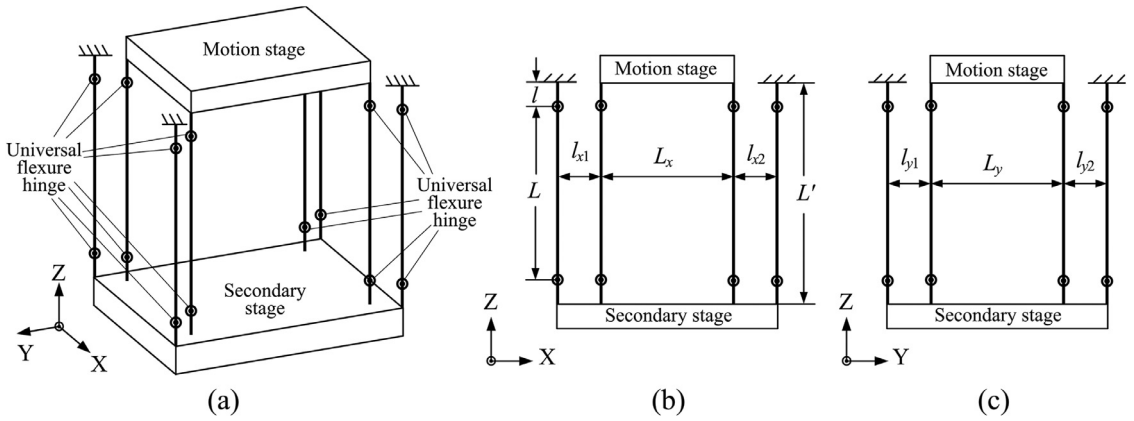

Fig. 4. The PRB model of 2-DCCPGM: (a) isometric view of the PRB model of 2-DCCPGM; (b) side view of 2-DCCPGM along the Y-axis; (c) side view of 2-DCCPGM along the X-axis.

However, this situation only occurs on the condition that the guiding displacement is small and the load of the 2-DOF spatial stage is too small to ignore. When the guiding displacement is relatively large and the load F_l cannot be ignored, a parasitic moment will be generated on the 2-DOF spatial stage, thus a translational error δ' will occur in the Z-axis, as shown in Fig. 3g.

From previous section, it is known that the 2-DOF spatial stage scarcely has parasitic rotation and parasitic translation in X-axis. That is because the 2-DOF spatial stage has the structure of CPF in X-axis. So, if a mechanism has the structure of CPF in both X-axis and Y-axis, it would be a perfect solution to all above mentioned problems. If we connect the motion stages and secondary stages of two identical 2-DOF spatial stages respectively, as shown in Fig. 3h, the newly created mechanism can be regarded as a CPF in Y-axis.

Based on above analysis, a novel 2-DOF compound compliant parallel-guiding mechanism is developed, as shown in Fig. 4a. All the 16 universal flexure hinges of 2-DCCPGM are the same. Fig. 4b and c indicate that the 2-DCCPGM has the structure of CPFs in both X-axis and Y-axis. And from Fig. 4a, the 2-DCCPGM can also be regarded as two reversely arranged FBCMs. So, the parasitic displacements of the motion stage and secondary stage will be equal in value and opposite in direction, when a driving force acts on the motion stage. Then, it can be considered that the newly designed mechanism does not generate parasitic displacements. From Eq. (10), the guiding displacement of the 2-DCCPGM can be derived as follows:

$$D_x = 2L\sin(\frac{F_xL}{8K_x}) \approx \frac{F_xL^2}{4K_x}, D_y = 2L\sin(\frac{F_yL}{8K_y}) \approx \frac{F_yL^2}{4K_y} \tag{11}$$

where F_x and F_y are the driving force applied on the motion stage in X-axis and Y-axis, respectively; K_x and K_y are the rotational stiffness coefficients along X-axis and Y-axis of the universal flexure hinges of the 2-DCCPGM, respectively.

Eq. (11) can be also written as:

$$D_x = \frac{F_x}{K_X}, D_y = \frac{F_y}{K_Y}, K_X = \frac{4K_x}{L^2}, K_Y = \frac{4K_y}{L^2} \tag{12}$$

where K_X and K_Y are the translational stiffness coefficients of 2-DCCPGM along X-axis and Y-axis, respectively.

From Eq. (12), it can be seen that the guiding displacements of 2-DCCPGM are proportional to the driving forces and inversely proportional to translational stiffness coefficients of 2-DCCPGM.

2.2. Dynamic modeling

The dynamic performance of 2-DCCPGM in the X-axis is considered first. The X-axis kinetic energy for 2-DCCPGM can be expressed as follows:

$$T = \frac{1}{2}Mv_x^2 = \frac{1}{2}m_1v_x^2 + \frac{1}{2}m_2v_{x2}^2 = (\frac{1}{2}m_1 + \frac{1}{8}m_2)v_x^2 \tag{13}$$

where M is the equivalent mass of 2-DCCPGM; m_1 and m_2 are the mass of the motion stage and the secondary stage, respectively; v_x and v_{x2} are the velocities of the motion stage and the secondary stage in the X-axis, respectively.

In addition, the elastic potential energy of 2-DCCPGM in the X-axis can be written as:

$$V = 16 \times \frac{1}{2}K_x(\varphi_y)^2 = \frac{2K_xx^2}{L^2} \tag{14}$$

where x is the output displacement of 2-DCCPGM in the X-axis; φ_y is the angular displacement of the flexure hinges of 2-DCCPGM along Y-axis.

Then, substituting Eqs. (13) and (14) into the Lagrange's equation

$$\frac{d}{dt}\left(\frac{\partial T}{\partial \dot{x}}\right) - \frac{\partial T}{\partial x} + \frac{\partial V}{\partial x} = F_x \tag{15}$$

allows the generation of the free-motion dynamic equation

$$\left(m_1 + \frac{1}{4}m_2\right)\ddot{x} + \frac{4K_x}{L^2}x = 0 \tag{16}$$

which gives the natural frequency of 2-DCCPGM in the X-axis in unit of Hertz

$$f_x = \frac{1}{2\pi}\sqrt{\frac{4K_x}{L^2\left(m_1 + \frac{1}{4}m_2\right)}} = \frac{1}{2\pi}\sqrt{\frac{4K_X}{m_1 + \frac{1}{4}m_2}}. \tag{17}$$

Similarly, the natural frequency (in unit of Hertz) of 2-DCCPGM in the Y-axis could also be obtained:

$$f_y = \frac{1}{2\pi}\sqrt{\frac{4K_y}{L^2\left(m_1 + \frac{1}{4}m_2\right)}} = \frac{1}{2\pi}\sqrt{\frac{4K_Y}{m_1 + \frac{1}{4}m_2}}. \tag{18}$$

From Eqs. (17) and (18), it can be seen that the natural frequencies of 2-DCCPGM are proportional to the square of translational stiffness coefficients of 2-DCCPGM.

Moreover, from Eq. (12), we can also notice that the translational stiffness coefficients of 2-DCCPGM are only related to the rotational stiffness coefficients of the flexure hinges (K_x and K_y) and the distance between the two flexure hinges of compliant beam (L).

In summary, K_x, K_y and L are the most important parameters of the 2-DCCPGM. These parameters should be designated carefully. Besides these parameters, people can determine the other dimensions of 2-DCCPGM based on their own needs, e.g., l, l_{x1}, l_{x2}, l_{y1}, l_{y2}, L_x and L_y in Fig. 4b and c.

3. 3-D modeling

The aim of this paper is to propose a new compliant mechanism with compact structure, long motion range and negligible parasitic displacements. So, some design constrains of the 3-D model of 2-DCCPGM should be taken into account.

The first constrain arises from the motion range

$$D_{\max} > 2\,\text{mm} \tag{19}$$

where $D_{\max}$ is the motion range of 2-DCCPGM both in the X-axis and Y-axis.

The second constrain is imposed by the requirement of compact structure

$$S_x \times S_y \times S_z < 100\,\text{mm} \times 100\,\text{mm} \times 100\,\text{mm} \tag{20}$$

where S_x, S_y and S_z are the size limits of the 3-D model of 2-DCCPGM in the X-axis, Y-axis and Z-axis, respectively. In addition, the designation of the size limits should also take into account the difficulty of machining.

3.1. Selection of flexure hinges

As discussed above, the performance of 2-DCCPGM is significantly related to the performance of the flexure hinges. Therefore, the selection of flexure hinges becomes the priority of designing a 3-D model of 2-DCCPGM.

Fig. 5 shows three different kinds of universal flexure hinges: parallel biaxial hinge, spherical hinge and serial biaxial hinge. Parallel biaxial hinge has compact structure, but stress concentration will occur on its four arris when it is deformed. Spherical hinge needs to be manufactured by turning, which is not suitable for fabricating the 2-DCCPGM monolithically. Serial biaxial hinge is a two-axis flexure hinge composed of two perpendicularly non-collocated flexure hinges. It is easy to fabricate and won't cause stress concentration, so it is adopted as the universal flexure hinges of 2-DCCPGM.

Due to the large motion requirement, the motion stage will be driven by a piezo motor. Given a piezo motor with the maximum driving force ($F_M = 50\,\text{N}$), the universal flexure hinges of 2-DCCPGM should be compliant enough so that the piezo motor is able to drive it. In addition, there are many different types of flexure hinges could be used in serial biaxial hinge, e.g., circular, elliptical, corner-filleted, and so on [31-34]. Among those flexure hinges, corner-filleted flexure hinge is the most compliant and induces the lowest stress, so it is adopted as the flexure hinges of serial biaxial hinge.

Moreover, in order to make the universal flexure hinge have the same stiffness both in the X-axis and Y-axis, the two corner-filleted flexure hinges of it have the same dimensions.

3.2. Structural design

Based on the elastic beam theory, the rotational stiffness coefficients along X-axis and Y-axis of the universal flexure hinges could be obtained

$$K_x = K_y = \frac{EI_c}{l_c} = \frac{Eb_c{t_c}^3}{12l_c} \tag{21}$$

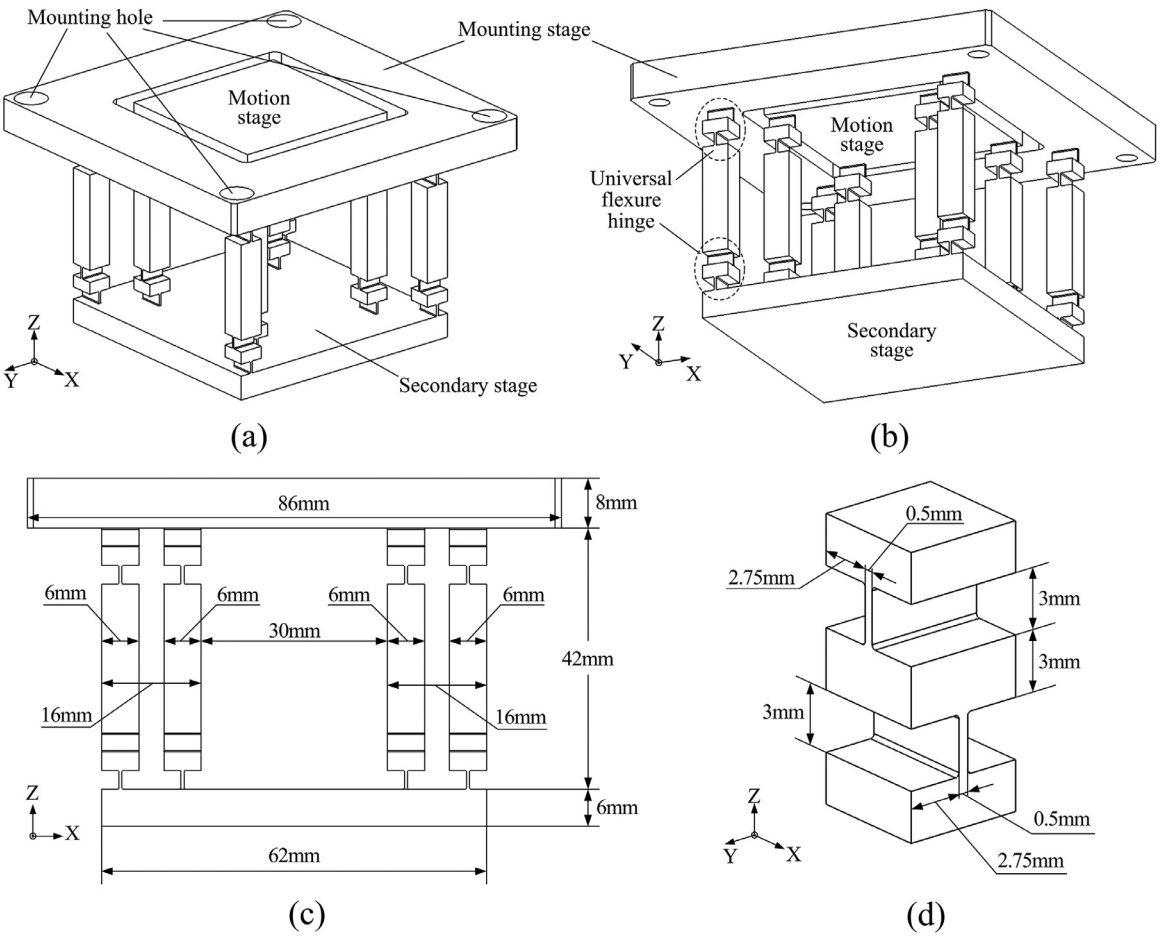

Fig. 5. Several types of universal flexure hinges could be used in 2-DCCPGM: (a) parallel biaxial flexure hinge; (b) spherical flexure hinge; (c) serial biaxial flexure hinge.

Table 1
Material properties of AW7075.

Young's modulus (GPa)	Poisson's ratio	Density (kg/mm^3)	Yield stress (MPa)
71	0.3	2.7×10^{-6}	503

where E is the Young's modulus of the material; I_c is the area moment of inertia of the corner-filleted flexure hinges; l_c,b_c and t_c are the length, the width and the thickness of the corner-filleted flexure hinges, respectively.

Due to the limitations of machining capacity, the thickness of the corner-filleted flexure hinges should be

$$t_c \geq 0.5\,\text{mm}. \tag{22}$$

In order to make the corner-filleted flexure hinge only have 1-DOF rotation capacity, b_c should be about ten times of t_c:

$$b_c \geq 5\,\text{mm}. \tag{23}$$

From Eq. (21), the elastic modulus of the material has significant influence on the rotational stiffness of flexure hinges. It means that the selection of material could affect the dimensions of the structure. In this paper, aluminum alloy AW7075 is chosen as material of the 2-DCCPGM, and the material properties are shown in Table 1.

From Eqs. (11), (19) and (20), the first design constrain can be expressed as

$$D_{\max} = \frac{3F_M L^2 l_c}{E b_c t_c^3} > 2\,\text{mm}. \tag{24}$$

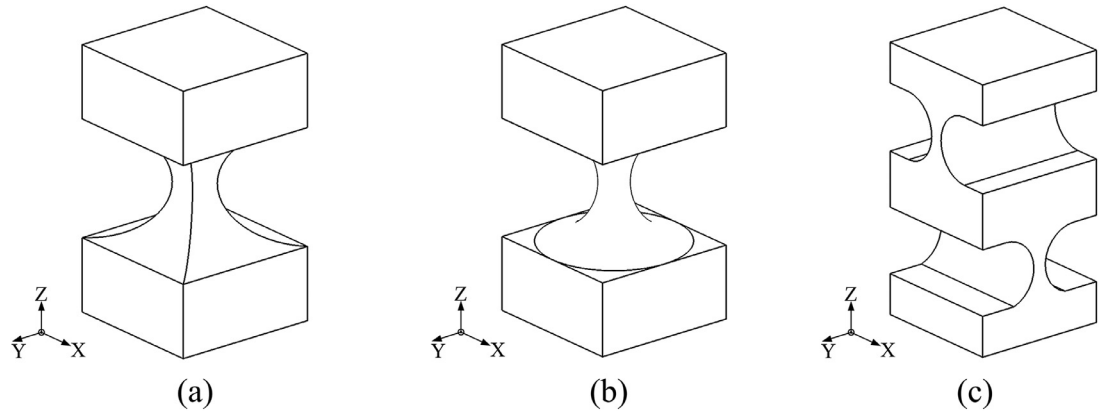

Fig. 6. 3-D model of 2-DCCPGM and its dimensions: (a) isometric view of 2-DCCPGM; (b) side upward view of 2-DCCPGM; (c) dimensions of 2-DCCPGM; (d) dimensions of the universal flexure hinges.

Table 2
The results of static FEA simulations.

Force status	Maximum stress (MPa)	Displacement of the motion stage in the X-axis (mm)	Displacement of the motion stage in the Y-axis (mm)	Displacement of the motion stage in the Z-axis (mm)
20 N in X-axis	336.334	2.7035	-2.9584×10^{-6}	3.8450×10^{-6}
20 N in Y-axis	342.458	-3.2911×10^{-5}	2.7003	2.5359×10^{-6}
20 N both in X-axis and Y-axis	401.112	2.7035	2.7003	6.3809×10^{-6}

For safety and durability, the maximum stress of the flexure hinges should be smaller than the yield stress as much as possible

$$\sigma_y > \sigma_{\max} = \frac{3F_M L}{b_c t_c^2} \tag{25}$$

where σ_y is the yield stress of the material, $\sigma_{\max}$ is the maximum stress of the flexure hinges.

And then, from Table 1 and Eqs. (20), (22), (23), (24) and (25), the unknown geometric parameters of the structure can be determined.

Based on above analysis, a 3-D model is built, as shown in Fig. 6a and b. Symmetrical structure is adopted in the 3-D model. The square motion stage is connected to the secondary stage by four compliant beams which are evenly distributed in the four corners of the motion stage, and the square secondary stage is connected to the mounting stage by another four compliant beams which are evenly distributed in the four corners of the secondary stage. All these eight compliant beams are totally the same, and they are all composed of rigid beams with universal flexure hinges at both ends. The dimensions of the 3-D model are shown in Fig. 6c.

Fig. 6d shows dimensions of universal flexure hinges which are adopted in the 3-D model.

4. FEA simulations

4.1. Static analysis

To verify the performance of the 2-DCCPGM, FEA simulations are carried out using an ANSYS software package. Element solid185 is chosen to build the model. And all the elements are tetrahedral-shaped elements. The element size is 1.2 mm. Since the deformation of the 2-DCCPGM mainly occurs at flexure hinges, the element size of the flexure hinges is defined as 0.2 mm. And in some critical parts, the element size is refined to 0.1 mm. The number of elements is over 1.4 million. First, the static performance of the 2-DCCPGM is evaluated using static structural FEA. The simulations are carried out by applying input forces on the motion stage in the X-axis and Y-axis. And 3-DOF translational constrains are added to the four mounting holes to restrict the mounting stage.

The deformation and the stress distribution of the 2-DCCPGM are illustrated in Fig. 7a and b, respectively, when 20 N driving force is applied on the motion stage in the X-axis. The deformation and the stress distribution of the 2-DCCPGM are illustrated in Fig. 7c and d, respectively, when 20 N driving force is applied on the motion stage in the Y-axis. And Fig. 7e and f show the deformation and the stress distribution of the 2-DCCPGM, respectively, when 20 N driving forces were applied on the motion stage both in X-axis and Y-axis. The results of static FEA simulations are shown in Table 2.

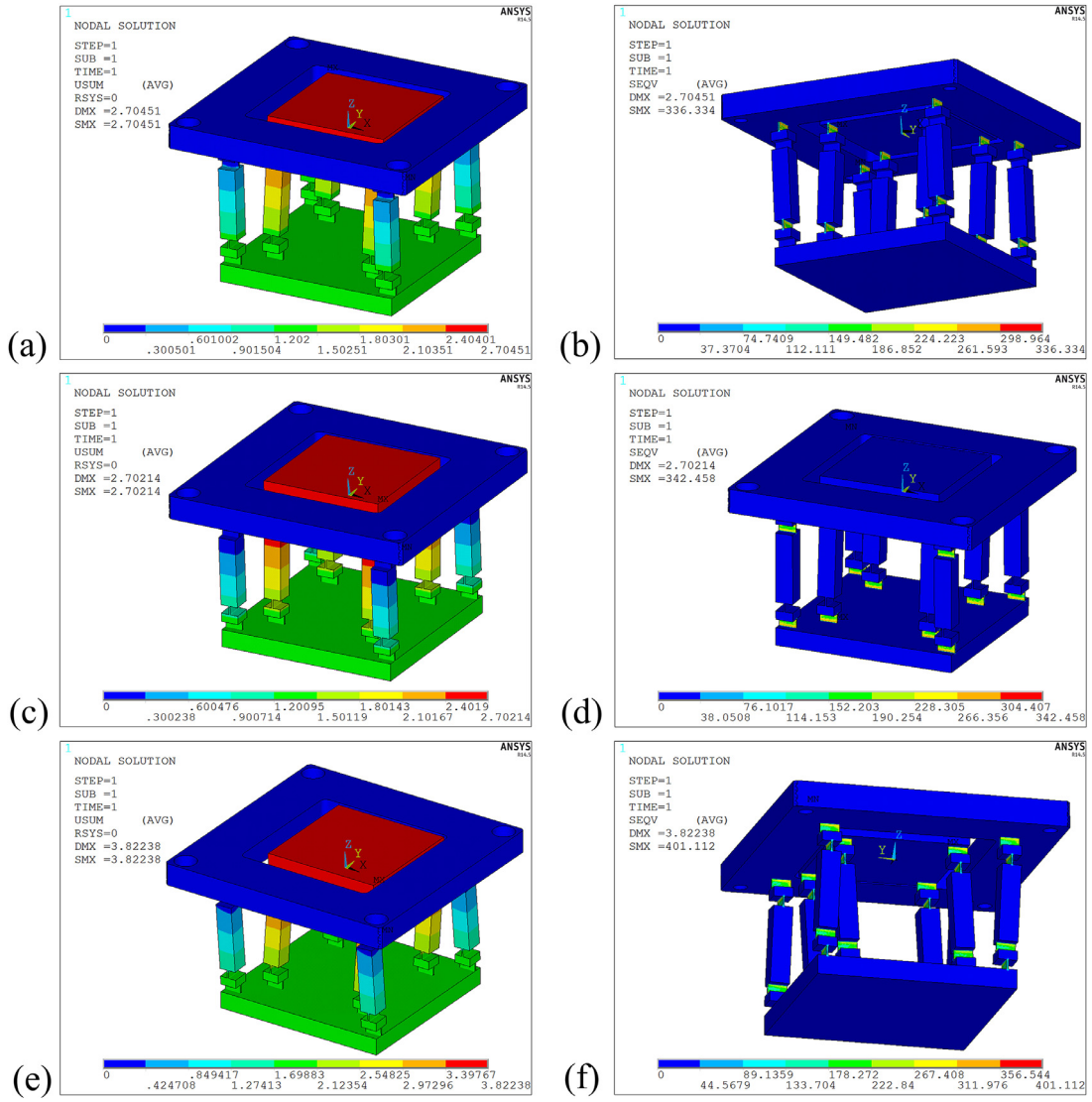

Fig. 7. The static FEA results of the 2-DCCPGM: (a) the deformation of the 2-DCCPGM when apply 20 N in X-axis; (b) the stress distribution of the 2-DCCPGM when apply 20 N in X-axis; (c) the deformation of the 2-DCCPGM when apply 20 N in Y-axis; (d) the stress distribution of the 2-DCCPGM when apply 20 N in Y-axis; (e) the deformation of the 2-DCCPGM when apply 20 N both in X-axis and Y-axis; (f) the stress distribution of the 2-DCCPGM when apply 20 N both in X-axis and Y-axis.

From Table 2, it can be seen that the 2-DCCPGM has very good guiding performance and the parasitic displacements are small enough to be neglected. Moreover, the maximum stresses are still less than the yield stress as the guiding displacements of the 2-DCCPGM reach 2.7 mm in both X-axis and Y-axis.

According to the dimension of corner-filleted flexure hinge in Fig. 6d and material properties in Table 1, we can get that $K_x = K_y = 1.479$ N m/rad from Eq. (21). And we can also get that $L = 33$ mm from Fig. 6c.

When 20 N driving forces were applied on the motion stage in both X-axis and Y-axis, from Eq. (11)

$$D_x = \frac{F_x L^2}{4K_x} = 3.68\,\text{mm}, D_y = \frac{F_y L^2}{4K_y} = 3.68\,\text{mm}. \tag{26}$$

It can be seen that the result based on the PRB model is larger than the FEA result. This is because the PRB model is based on many assumptions, which can cause the loss of accuracy. But the PRB model is still useful as an auxiliary tool in structural designing of the 2-DCCPGM.

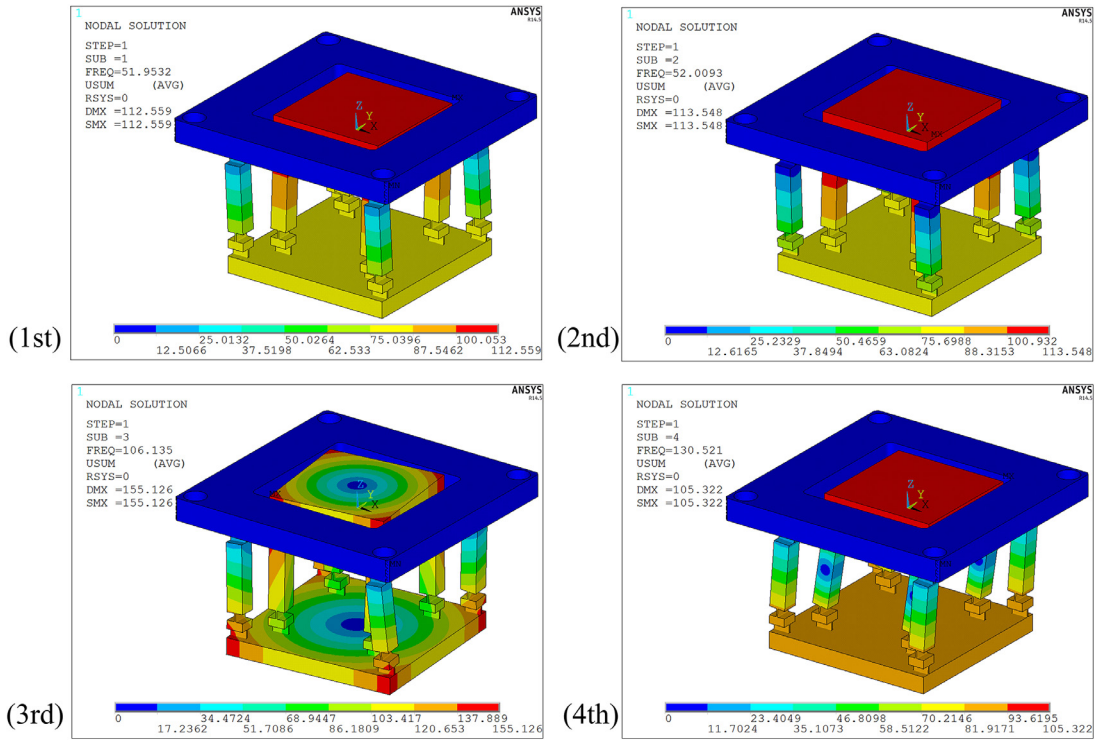

Fig. 8. The first-four mode shapes of the 2-DCCPGM.

Table 3
The first-four resonant frequencies of the 2-DCCPGM.

First mode (Hz)	Second mode (Hz)	Third mode (Hz)	Fourth mode (Hz)
51.953	52.009	106.135	130.521

4.2. Dynamic analysis

Then, the FEA modal simulations are carried out to evaluate the dynamic performance of the 2-DCCPGM. The first-four mode shapes are shown in Fig. 8, and the first-four resonant frequencies are shown in Table 3.

By observing the modal results, one can notice that the first-two resonant frequencies are very close and mode shapes of them are the same. It is due to the fact that the 3-D model of the 2-DCCPGM, which is built in previous section, has a symmetrical structure.

In order to compare with the FEA result, the dynamic analysis based on PRB model is taken. According to the finite element model of the 2-DCCPGM, the mass of the motion stage and the secondary stage can be obtained

$$m_1 = 0.038\,\text{kg}, \qquad m_2 = 0.062\,\text{kg}. \tag{27}$$

From Eqs (17), (18) and (21), the analytical natural frequencies of the 2-DCCPGM are

$$f_1 = f_2 = 50.716\,\text{Hz}. \tag{28}$$

It is found that the analytical results are in good agreement with simulation results.

5. Prototype fabrication and experiment

A prototype of the 2-DCCPGM has been fabricated, as shown in Fig. 9a. This prototype is monolithically manufactured from an aluminum alloy AW7075 block. The external shape is fabricated on a computer numerical controlled (CNC) milling machine, and a CNC assisted wire electrical discharge machine (WEDM) is utilized to manufacture all the flexure hinges.

The setup of the experimental system is shown in Fig. 9b and c. Two piezo motors (model: PZA12, produced by Newport) are employed as motion generators. These piezo motors could ensure highly reliable motion with 30 nm sensitivity over 12.5 mm travel, and have no loss of position when power is removed. The motion stage is driven directly by piezo motors. The piezo motor controllers (model PZC200, from Newport) are utilized to drive those piezo motors. Capacitive sensors

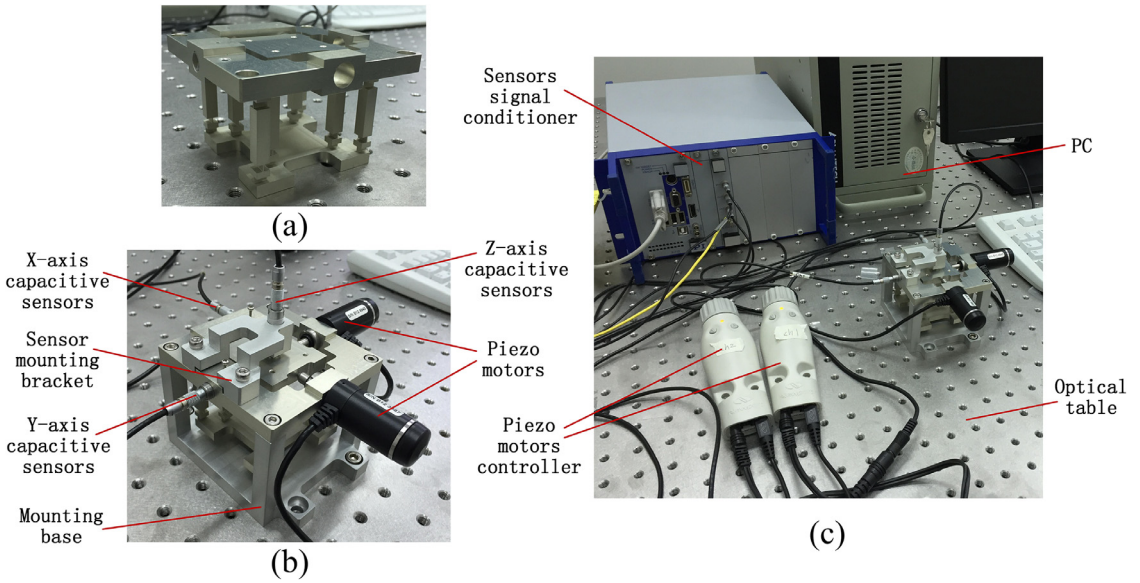

Fig. 9. Manufactured prototype and the setup of experimental system.

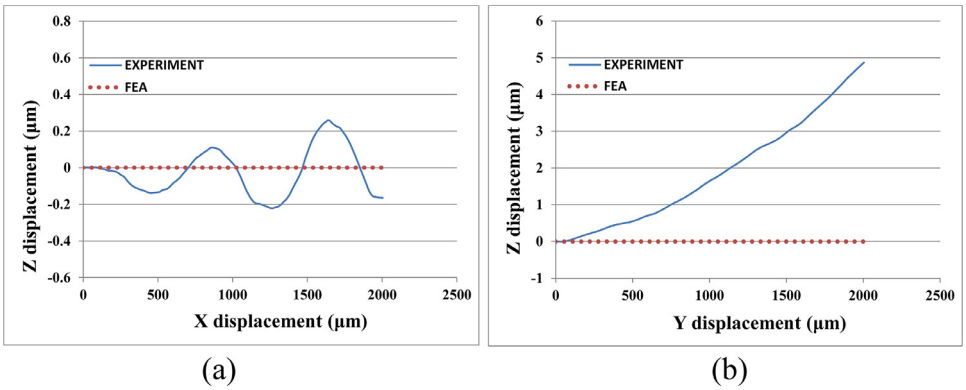

Fig. 10. Results comparisons of experiment and FEA: (a) Z-axis displacement while driving in the X-axis; (b) Z-axis displacement while driving in the Y-axis.

(model: D-E20.200, from Physik Instrumente) are adopted to measure the displacement of the motion stage. After calibration by manufacturer, this capacitive sensor could have 4 different measuring ranges, 200 μm, 500 μm, 1000 μm, 2000 μm, by signal amplification. The Z-axis capacitive sensor adopts the range of 200 μm to measure the parasitic displacement, and the X-axis and Y-axis capacitive sensors adopt the range of 2000 μm to measure the guiding displacements. The signal conditioner (model: E-E12.009, from Physik Instrumente) is used to process the position signal from all three capacitive sensors.

The experimental results of the 2-DCCPGM are shown in Fig. 10, when the 2-DCCPGM is driven along the X-axis and Y-axis, respectively. From Fig. 10(a), the displacement along Z-axis is about ±0.2 μm over a 2 mm range of travel in X-axis, and then the guiding linearity of the 2-DCCPGM along X-axis is about 0.02%. Furthermore, one can observe that the curve of the Z-axis displacement fluctuates around the initial position and has no obvious pattern. Then, we can speculate that what the curve indicated is the surface shape of the motion stage of the 2-DCCPGM rather than the parasitic displacement of the guiding motion. That is because the surface of motion stage is manufactures by a milling machine, as motioned above, the machining marks have been left on the surface. Moreover, the flatness of the surface may also have influence on the measuring result over a 2 mm range of travel.

From Fig. 10(b), the Z-axis displacement is about 5 μm over a 2 mm range of travel in Y-axis, and then the guiding linearity of the 2-DCCPGM along Y-axis is about 0.25%. It is easy to notice that the guiding linearity of the 2-DCCPGM along Y-axis is much larger than the guiding linearity along X-axis. However, it is mainly because of the machining deviation of the universal flexure hinges.

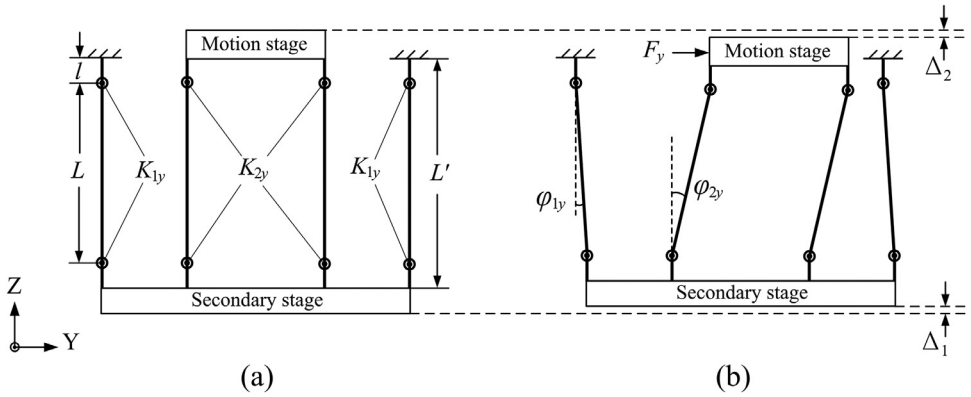

Fig. 11. Parasitic displacement caused by stiffness differences of the flexure hinges: (a) The PRB model of the 2-DCCPGM with stiffness differences on the flexure hinges; (b) parasitic displacement caused by stiffness differences of the flexure hinges.

The side view of a PRB model of 2-DCCPGM with machining deviation is shown in Fig. 11(a). The stiffness of flexure hinges between the mount stage and the secondary stage K_{1y} is different from the stiffness of flexure hinges between the motion stage and the secondary stage K_{2y}, and $K_{1y} > K_{2y}$. Fig. 11(b) shows the deformation of the 2-DCCPGM when the motion stage is driven by a force F_y along Y-axis.

From Eq. (8), the rotation angles of the flexure hinges of the 2-DCCPGM, which are shown in Fig. 11(b), can be derived

$$\varphi_{1y} = \frac{F_y L}{8K_{1y}}, \varphi_{2y} = \frac{F_y L}{8K_{2y}}. \tag{29}$$

From Fig. 11(b), the parasitic displacements of the secondary stage and the motion stage are

$$\Delta_1 = L(1 - \cos\varphi_{1y}), \Delta_2 = L(1 - \cos\varphi_{2y}) - \Delta_1 = L(\cos\varphi_{1y} - \cos\varphi_{2y}). \tag{30}$$

From trigonometric function formula, Δ_2 can be expressed as

$$\Delta_2 = L(\cos\varphi_{1y} - \cos\varphi_{2y}) = L(-2\sin(\frac{\varphi_{1y} + \varphi_{2y}}{2})\sin(\frac{\varphi_{1y} - \varphi_{2y}}{2})) \approx L\frac{(\varphi_{1y} + \varphi_{2y})(\varphi_{2y} - \varphi_{1y})}{2} = L\frac{\varphi_{2y}^2 - \varphi_{1y}^2}{2}. \tag{31}$$

Substituting Eq. (29) into Eq. (31), the parasitic displacement of and the motion stage could be obtained by following equation

$$\Delta_2 = L\frac{\varphi_{2y}^2 - \varphi_{1y}^2}{2} = L\frac{F_y^2 L^2 K_{1y}^2 - F_y^2 L^2 K_{2y}^2}{2(8^2 K_{1y}^2 K_{2y}^2)} = \frac{F_y^2 L^3 (K_{1y}^2 - K_{2y}^2)}{128 K_{1y}^2 K_{2y}^2}. \tag{32}$$

By observing Eq. (32), it can be seen that the parasitic displacement is proportional to the square of the driving force. Moreover, from Eq. (12), the guiding displacement is proportional to the driving force. So, the parasitic displacement is proportional to the square of the guiding displacement. From Fig. 11(b), one can observe that the curve of Z-axis displacement is a downward convex curve and keeps ascending with the increase of guiding displacement. And the shape of the curve is consistent with Eq. (32).

Based on the measuring results and above analysis, we can say that the 2-DCCPGM has satisfactory guiding performance.

6. Conclusions

Based on the analysis of the 2-DOF spatial stage, a novel 2-DOF compound compliant parallel guiding mechanism is proposed in this paper. This mechanism can be considered as two identical 2-DOF spatial stages whose motion stages and secondary stages are connected respectively, which makes 2-DCCPGM have the structure of CPF in both X-axis and Y-axis. And the 2-DCCPGM can also be regarded as two reversely arranged FBCMs, thus the parasitic displacements of these FBCMs will be equal in value and opposite in direction, when a driving force acts on the motion stage. It means that the parasitic displacement of the motion stage equals to zero. So, we have drawn a conclusion that the 2-DCCPGM does not generate parasitic displacements. The relationship between the guiding displacements and the driving forces has been obtained, based on the PRB model of the 2-DCCPGM. And the dynamic analysis is taken as well, and the formulas of resonant frequencies are obtained. Based on these analyses, the rotational stiffness coefficients of the flexure hinges and the distance between the two flexure hinges of compliant beam are demonstrated to be the most important parameters of 2-DCCPGM. And the design guideline of the 2-DCCPGM is also expounded. Moreover, the FEA simulations are carried out to analysis the guiding capability and dynamic performance of the 2-DCCPGM. The results of the FEA static simulations have confirmed that the 2-DCCPGM barely generates parasitic displacements. And the results of FEA modal simulations are in good agreement with

the analytical results. After experimental studies, the 2-DCCPGM has been proved to have satisfactory guiding performance. Moreover, the experiment results have also revealed that the machining deviation of the flexure hinges of 2-DCCPGM could cause parasitic displacements and reduce the guiding linearity of the 2-DCCPGM.

In this paper, parasitic displacements and guiding linearity of the 2-DCCPGM are preliminarily analyzed. And the impact caused by machining deviation and torsional behavior of the 2-DCCPGM can be researched in related future works.

Acknowledgments

This work was supported by the 02 Major National Science and Technology Projects of China (2009ZX02202-005).

References

[1] G. Schitter, K.J. Åström, B.E. DeMartini, P.J. Thurner, K.L. Turner, P.K. Hansma, Design and modeling of a high-speed AFM-scanner, IEEE Trans. Control Syst. Technol. 15 (2007) 906–915.
[2] K. Obata, A. EL-Tamer, L. Koch, U. Hinze, B.N. Chichkov, High-aspect 3D two-photon polymerization structuring with widened objective working range (WOW-2PP), Light Sci. Appl. doi:10.1038/lsa.2013.72.
[3] T. Matsuyama, Y. Ohmura, D.M. Williamson, The lithographic lens: its history and evolution, Proc. of SPIE 6154 (2006) 615403.
[4] S.-K. Ro, S. Kim, Y. Kwak, C.H. Park, A linear air bearing stage with active magnetic preloads for ultraprecise straight motion, Precis. Eng. 34 (2010) 186–194.
[5] Y.-L. Sun, W.-F. Dong, L.-G. Niu, T. Jiang, D.-X. Liu, L. Zhang, Y.-S. Wang, Q.-D. Chen, D.-P. Kim, H.-B. Sun, Protein-based soft micro-optics fabricated by femtosecond laser direct writing, Light Sci. Appl. doi:10.1038/lsa.2014.10.
[6] L.L. Howell, Compliant Mechanisms, McGraw-Hill, New York, 2009.
[7] Y. Luo, W. Liu, Analysis of the displacement of distributed compliant parallel-guiding mechanism considering parasitic rotation and deflection on the guiding plate, Mech. Mach. Theory 80 (2014) 151–165.
[8] Y. Singh, V. Vinoth, Y.R. Kiran, J.K. Mohanta, S. Mohan, Inverse dynamics and control of a 3-DOF planar parallel (U-shaped 3-PPR) manipulator, Robot, Comput.-Integr. Manuf. 34 (2015) 164–179.
[9] L. Rubbert, R. Bitterli, N. Ferrier, S. Fifanski, I. Vardi, S. Henein, Isotropic springs based on parallel flexure stages, Precis. Eng. 43 (2016) 132–145.
[10] Z. Ni, D. Zhang, Y. Wu, Y. Tian, M. Hu, Analysis of parasitic motion in parallelogram compliant mechanism, Precis. Eng. 34 (2010) 133–138.
[11] K.-B. Choi, J.J. Lee, S. Hata, A piezo-driven compliant stage with double mechanical amplification mechanisms arranged in parallel, Sens. Actuators A 125 (2010) 173–181.
[12] Y. Yue, F. Gao, X. Zhao, Q.J. Ge, Relationship among input-force, payload, stiffness and displacement of a 3-DOF perpendicular parallel micro-manipulator, Mech. Mach. Theory 45 (2010) 756–771.
[13] K.-Q. Qi, Y. Xiang, C. Fang, Y. Zhang, C.-S. Yu, Analysis of the displacement amplification ratio of a bridge-type mechanism, Mech. Mach. Theory 87 (2015) 45–56.
[14] S. Polit, J. Dong, Development of a high-bandwidth XY nanopositioning stage for high-rate micro-/nanomanufacturing, IEEE/ASME Trans. Mechatron. 16 (2011) 724–733.
[15] F. Villar, J. David, G. Genevès, 75 mm stroke flexure stage for the LNE watt balance experiment, Precis. Eng. 35 (2011) 693–703.
[16] B.J. Kenton, K.K. Leang, Flexure design using metal matrix composite materials: nanopositioning example, in: Proceedings of 2012 IEEE International Conference on Robotics and Automation (ICRA), IEEE, 2012, pp. 4768–4773.
[17] Z. Guo, Y. Tian, X. Liu, B. Shirinzadeh, F. Wang, D. Zhang, An inverse Prandtl-Ishlinskii model based decoupling control methodology for a 3-DOF flexure-based mechanism, Sens. Actuators A 230 (2015) 52–62.
[18] P. Liu, P. Yan, A new model analysis approach for bridge-type amplifiers supporting nano-stage design, Mech. Mach. Theory 99 (2016) 176–188.
[19] S. Noveanu, N. Lobontiu, J. Lazaro, D. Mandru, Substructure compliance matrix model of planar branched flexure-hinge mechanisms: design, testing and characterization of a gripper, Mech. Mach. Theory 91 (2015) 1–20.
[20] Y. Luo, W. Liu, L. Wu, Analysis of the displacement of lumped compliant parallel-guiding mechanism considering parasitic rotation and deflection on the guiding plate and rigid beams, Mech. Mach. Theory 91 (2015) 50–68.
[21] X. Yang, W. Li, Y. Wang, L. Zhang, G. Ye, X. Su, Analysis of the displacement of complaint double parallel four-bar mechanism, in: Proceedings of 2009 4th IEEE Conference on Industrial Electronics and Applications (ICIEA), IEEE, 2009, pp. 2760–2763.
[22] J.W. Ryu, D.-G. Gweon, Error analysis of a flexure hinge mechanism induced by machining imperfection, Precis. Eng. 21 (1997) 83–89.
[23] S. AWTAR, Synthesis and Analysis of Parallel Kinematic XY Fexure Mechanisms, Massachusetts Institute of Technology, Boston, 2004.
[24] Q. Xu, New flexure parallel-kinematic micropositioning system with large workspace, IEEE Trans. Robot. 28 (2012) 478–491.
[25] G. Hao, X. Kong, A novel large-range XY compliant parallel manipulator with enhanced out-of-plane stiffness, J. Mech. Des. 134 (2012) 061009.
[26] X. Tang, I.-M Chen, A large-displacement 3-DOF flexure parallel mechanism with decoupled kinematics structure, in: Proceedings of 2006 IEEE/RSJ International Conference on Intelligent Robots and System (IROS), IEEE, 2006, pp. 1668–1673.
[27] Y. Qin, B. Shirinzadeh, Y. Tian, D. Zhang, Design issues in a decoupled XY stage: Static and dynamics modeling, hysteresis compensation, and tracking control, Sens. Actuators A 194 (2013) 95–105.
[28] J.-P. Bacher, S. Bottinelli, J.-M. Breguet, R. Clavel, Delta^3: design and control of a flexure hinges mechanism, Proc. SPIE 4568 (2001) 135–146.
[29] Q. Xu, Y. Li, Novel design of a totally decoupled flexure-based XYZ parallel micropositioning stage, in: 2010 IEEE/ASME International Conference on Advanced Intelligent Mechatronics (AIM), IEEE, 2010, pp. 866–871.
[30] G. Hao, Towards the design of monolithic decoupled XYZ compliant parallel mechanisms for multi-function applications, Mech. Sci. 4 (2013) 291–302.
[31] W. Xu, T. King, Flexure hinges for piezoactuator displacement amplifier: flexibility, accuracy and stress conditions, Precis. Eng. 19 (1996) 4–10.
[32] S.T. Smith, V.G. Badami, J.S. Dale, Y. Xu, Elliptical flexure hinges, Rev. Sci. Instrum. 68 (1997) 1474–1483.
[33] P.P. Valentini, E. Pennestri, Elasto-kinematic comparison of flexure hinges undergoing large displacement, Mech. Mach. Theory 110 (2017) 50–60.
[34] S. Linß, P. Schorr, Lena Zentner, General design equations for the rotational stiffness, maximal angular deflection and rotational precision of various notch flexure hinges, Mech. Sci. 8 (2017) 29–49.

Ke-qi Qi received his B.Eng. degree and M.Sc. degree in mechanics of engineering from Jilin University in 2007 and 2009, respectively. He is working as an assistant researcher at State Key Laboratory of Applied Optics, Changchun Institute of Optics, Fine Mechanics and Physics, Chinese Academy of Science. His research interests include precision mechanisms, robot system designing and optical device.

Ya-lin Ding received his Bachelor's degree from Jilin University of Technology in 1987, and received his Master's degree from Northeastern University in 1994. He is working as a research fellow at the Key Laboratory of Airborne Optical Imaging and Measurement, Changchun Institute of Optics, Fine Mechanics and Physics, Chinese Academy of Science. His research interests include air-borne remote sensing camera and stable imaging technology.

Yang Xiang received his B.S. degree in physics in 1985 and M.Sc. degree in theoretical physics in 1988, both from Northeast Normal University, China. He received his Ph.D. in optics in 1998 from Changchun Institute of Optics, Fine Mechanics and Physics, Chinese Academy of Science in 1998. He is working as a research fellow at the State Key Laboratory of Applied Optics, Changchun Institute of Optics, Fine Mechanics and Physics, Chinese Academy of Science. His research interests include optical testing and imaging spectrometry.

Chao Fang received his Bachelor's degree in science and technology of optoelectronics from Tianjin University in 2007, and Master's degree in optical engineering from Tianjin University in 2009. He is working as an assistant researcher at State Key Laboratory of Applied Optics, Changchun Institute of Optics, Fine Mechanics and Physics, Chinese Academy of Science. His research interests include optical testing and optical measurements.

Yang Zhang is a research fellow at Research Institute of Zhejiang University-Taizhou. He received his B.S. and Ph.D. in Mechatronics Engineering from Zhejiang University in 2005 and 2011, respectively. Now, his research interests are mechatronics, robotics and intelligent system.